J. Fluid Mech. (1997), *vol.* 340, *pp.* 101–128. Printed in the United Kingdom

© 1997 Cambridge University Press

Analytical investigation of two-dimensional unsteady shock-on-shock interactions

By H. LI AND G. BEN-DOR

Pearlstone Center for Aeronautical Engineering Studies, Department of Mechanical Engineering, Ben-Gurion University of the Negev, Beer Sheva, Israel

(Received 24 June 1996 and in revised form 6 September 1996)

The unsteady inviscid two-dimensional flow field and the wave configurations which result when a supersonic vehicle strikes a planar oblique shock wave were modelled and analytically predicted using some approximations and simplifying assumptions. Based on the two- and three-shock theories together with the geometric shock dynamics theory, both regular (windward) and irregular (leeward) shock-on-shock (S-O-S) interactions were investigated, and the transition criterion between them was suggested. For the case of regular S-O-S interaction, the transmitted shock wave reflects over the vehicle body surface either as a regular (RR) or a Mach reflection (MR) depending on the inclination angle and the strength of the impingement shock wave. A pronounced peak surface pressure jump was found to exist during the transition from RR to MR. A RR$\leftrightarrow$MR transition criterion when the flow ahead of the shock pattern is not quiescent was proposed. Predictions based on the model developed here are superior to those of approximate theories when compared to the available experimental data and numerical simulations.

1. Introduction

The interest in better understanding the unsteady flow field that results when a supersonic vehicle intercepts a planar oblique shock wave travelling in the opposite direction was initiated in the early 1960s. The interaction of the oblique shock wave with the vehicle bow shock wave was termed in the literature a shock-on-shock (S-O-S) interaction. The study of S-O-S interaction today is of interest for both theoretical and practical reasons.

Two examples of S-O-S interactions are shown schematically in figure 1. In figure 1(*a*), a supersonic aircraft (drawn for simplicity as a wedge) travels towards an explosion-generated blast wave. In figure 1(*b*), two supersonic aircrafts fly in opposite directions and pass near one another.

Attention was focused on the S-O-S interaction as part of the need to determine the strong blast-induced transient pulse produced at the surface of the supersonic vehicle because of the belief that the forces generated could be structurally damaging, and to answer the question of whether such an encounter could induce high-frequency disturbances capable of destroying the internal structure or appended equipment.

A brief well-written summary of the developments in the study of S-O-S interactions, since one of the first theoretical works by Smyrl (1963), is given in Kutler, Sakell & Aiello (1975), who numerically investigated the two-dimensional S-O-S interaction. In a successive study, Kutler & Sakell (1976) presented a numerical investigation of the three-dimensional S-O-S interaction.

The pre-interaction flow fields in an inertial (laboratory) frame of reference and in

https://doi.org/10.1017/S0022112097005326 Published online by Cambridge University Press

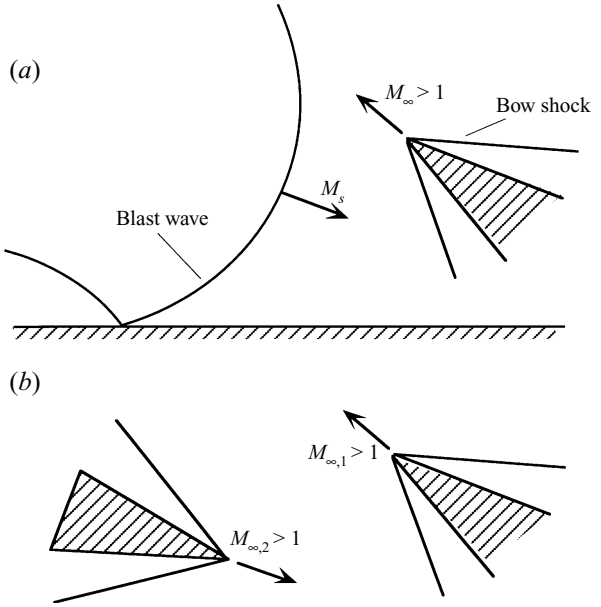


FIGURE 1. Examples of S-O-S problems: (*a*) an interception of a supersonic vehicle with a blast wave; (*b*) an encounter between two supersonic vehicles travelling in opposite directions.

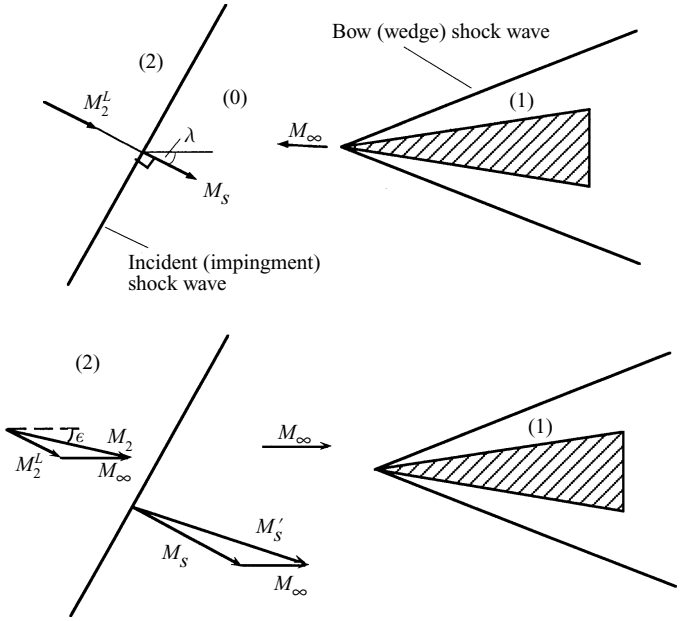


FIGURE 2. Definition of the flow parameters and domains in (*a*) a laboratory frame of reference and (*b*) a frame of reference attached to a travelling wedge.

wedge (i.e. supersonic vehicle)-fixed coordinates are shown in figures 2(*a*) and 2(*b*), respectively. An incident (impingement) shock wave, whose intensity is M_s, is seen to propagate from left to right towards a quiescent flow region (0). The incident-shock-induced flow region is (2) and its flow Mach number is M_2^L. In addition, a supersonic wedge whose Mach number is M_∞ is seen to propagate from right to left. The bow-

https://doi.org/10.1017/S0022112097005326 Published online by Cambridge University Press

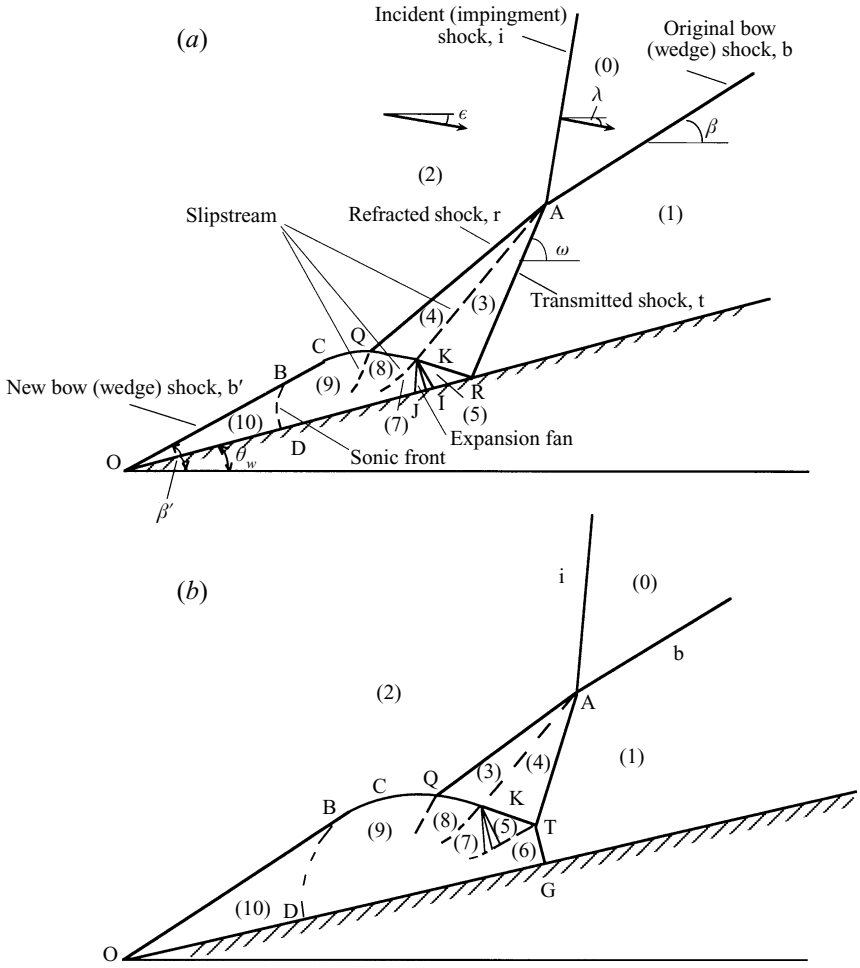


FIGURE 3. Schematic illustration of the wave configuration and the flow field of a regular S-O-S interaction and definition of the flow parameters and the flow domains. (*a*) Regular reflection on the wedge surface; (*b*) Mach reflection on the wedge surface.

shock-induced flow region is (1). (Note that in general the angle of attack of the wedge is not necessarily zero and hence the lower and the upper bow shocks can have different angles of incidence (i.e. strengths).) By superimposing, on the flow field shown in figure 2(*a*), a velocity equal and opposite to that of the supersonic wedge, the flow field shown in figure 2(*b*) is obtained. In this case of wedge-fixed coordinates, the wedge is stationary, the flow Mach number in region (1) is M_∞ and the flow Mach number behind the incident shock wave is M_2. Its orientation relative to the horizontal direction is ϵ.

The interaction of the incident and bow shock waves can lead, in general, to two types of S-O-S interaction, namely regular and irregular. Schematic illustrations of these two types of interaction, which are consistent with experimental observations and numerical simulations, are shown in figures 3 and 4, respectively. Detailed descriptions of the wave configurations and the associated flow fields are given in subsequent sections. For the regular S-O-S interaction shown in figure 3, which usually occurs in the windward side of a flying vehicle, the region of the flow field of most interest is at

https://doi.org/10.1017/S0022112097005326 Published online by Cambridge University Press

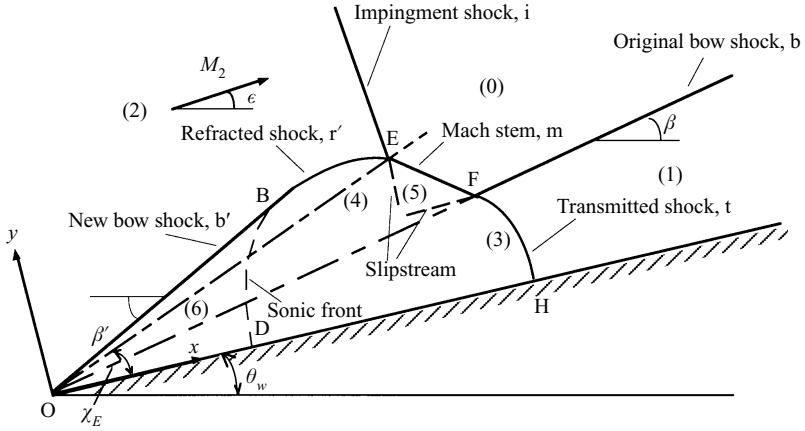


FIGURE 4. Schematic illustration of the wave configuration and the flow field of an irregular S-O-S interaction and definition of the flow parameters and the flow domains.

the body in the vicinity of the transmitted shock wave. This shock wave can reflect regularly (regular reflection) or irregularly (Mach reflection), depending on its strength and orientation. Major interest is given to the incident shock angle that yields the transition between regular and Mach reflection, for it is this encounter angle that results in the largest surface pressure at the body. Regarding the irregular S-O-S interaction, the aim of this study is to predict the trajectory angle of the intersection point as well as the transition criterion between the regular and the irregular S-O-S interactions.

Each of the existing theoretical approaches (e.g. Smyrl 1963; Blankenship 1964; Miles 1965; Inger 1966; Hudgins & Friedman 1973), involves simplifying assumptions about the S-O-S interaction flow field, for instance weak blast waves, thin or slender vehicles, replacement of curved shock waves by straight ones, etc. For an experimental investigation, it is extremely difficult to set up a given encounter. The numerical simulations have the drawbacks of the high resolution of wave configurations and considerable CPU time cost for the S-O-S interaction which contains complex wave systems and a number of independent variables.

This study attempts to analytically formulate the S-O-S interaction for any set of initial conditions without the simplifications used in the earlier theoretical approaches, and to get a better understanding of the physical mechanism of the S-O-S interaction. In addition, the S-O-S interactions provide the environment where two moving shock waves can irregularly intersect, and the transmitted shock wave reflects both regularly and irregularly over the surface in the flow ahead of itself. In the present study, transition criteria for both regular/irregular S-O-S interaction and regular/Mach reflection are proposed.

2. The present study

2.1. *Analysis of the wave configuration and flow field*

The regular S-O-S interaction can be subdivided into two types whose wave configurations are shown in figure 3. In both wave configurations, the incident (i) and bow (b) shock waves intersect at point A. As a result, the bow shock wave is refracted and the incident shock wave is transmitted. The flow field around the interaction point A is complemented by a slipstream which separates the flow fields behind the refracted

https://doi.org/10.1017/S0022112097005326 Published online by Cambridge University Press

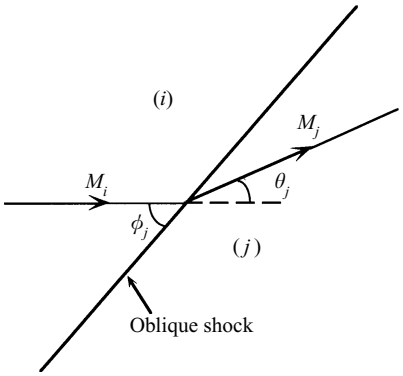


FIGURE 5. Definition of the parameters across an oblique shock wave.

(r) and transmitted (t) shock waves (regions (4) and (3), respectively). Note also that owing to the change in the flow conditions at the leading edge of the wedge a new bow shock wave is formed. As mentioned earlier, the transmitted shock wave (t) can reflect over the wedge surface either as a regular reflection (RR), as shown in figure 3(*a*), or as a Mach reflection (MR), as shown in figure 3(*b*). The definition of the flow domains and relevant parameters is also shown on figures 3(*a*) and 3(*b*).

The flow field around point K, where the reflected shock wave (RK of the RR shown in figure 3*a* or TK of the MR shown in figure 3*b*) intersects the primary slipstream emanating from point A, is complemented by a transmitted reflected shock wave, KQ, an expansion fan and a secondary slipstream. The curved transmitted reflected shock wave KQ interacts with the refracted shock wave (r) at point Q. The interaction results in a new stronger curved shock wave, QC, complemented by a slipstream emanating from point Q. The curved shock wave QC and the new bow shock wave interact and smoothly merge at point C. The downstream disturbances can reach point B. The arc BD shown in figures 3(*a*) and 3(*b*) is a sonic line. The part of the new bow shock wave, OB, is straight, since it is not caught up by any disturbance.

The irregular S-O-S interaction results in the wave configuration shown in figure 4. Unlike the regular S-O-S interaction wave configurations, here the incident and the bow shock waves do not intersect. Instead, they become parts of the two triple points, E and F, which are bridged by a common Mach stem (m) complemented by two slipstreams emanating from them. The transmitted shock wave (t) is smoothly turned to become perpendicular to the wedge surface. The refracted shock wave (r′) interacts with the new bow shock wave (b′) to result a wave configuration similar to that shown in figure 3 for the regular S-O-S interaction case.

The solution of the unsteady S-O-S interactions is based on the fact that the flow field is self-similar with respect to time. This is because no characteristic length is associated with the body and the incident shock wave is planar. Therefore, by applying the appropriate self-similar transformation to the unsteady gasdynamic equations, the unsteady problem can be made steady and be solved analytically.

2.2. *General governing equations for an oblique shock wave*

Consider figure 5 where an oblique shock wave is schematically shown. The flow states ahead and behind it are (*i*) and (*j*), respectively. The angle of incidence between the oncoming flow, whose Mach number is M_i, and the oblique shock wave is ϕ_j. While passing through the oblique shock wave the flow streamline is deflected by an angle of θ_j.

https://doi.org/10.1017/S0022112097005326 Published online by Cambridge University Press

The conservation equations relating states (i) and (j) for a steady inviscid flow of a perfect gas are (for details see Ben-Dor 1991)

conservation of mass

$$\rho_i u_i \sin\phi_j = \rho_j u_j \sin(\phi_j - \theta_j), \tag{1a}$$

conservation of normal momentum

$$P_i + \rho_i u_i^2 \sin^2\phi_j = P_j + \rho_j u_j^2 \sin^2(\phi_j - \theta_j), \tag{1b}$$

conservation of tangential momentum

$$\rho_i \tan\phi_j = \rho_j \tan(\phi_j - \theta_j), \tag{1c}$$

conservation of energy

$$\frac{\gamma}{\gamma-1}\frac{P_i}{\rho_i} + \frac{1}{2}u_i^2 \sin^2\phi_j = \frac{\gamma}{\gamma-1}\frac{P_j}{\rho_j} + \frac{1}{2}u_j^2 \sin^2(\phi_j - \theta_j), \tag{1d}$$

where u is the flow velocity, P is the pressure, ρ is the density and γ is the specific heat capacities ratio. The above equations can be combined to read

$$\theta_j = F(\gamma, M_i, \phi_j) = \arctan\left[\frac{2\cot\phi_j(M_i^2\sin^2\phi_j - 1)}{M_i^2(\gamma + \cos 2\phi_j) + 2}\right], \tag{2a}$$

$$M_j = G(\gamma, M_i, \phi_j) = \frac{\{1 + (\gamma-1)M_i^2\sin^2\phi_j + [\frac{1}{4}(\gamma+1)^2 - \gamma\sin^2\phi_j]M_i^4\sin^2\phi_j\}^{1/2}}{[\gamma M_i^2\sin^2\phi_j - \frac{1}{2}(\gamma-1)]^{1/2}[\frac{1}{2}(\gamma-1)M_i^2\sin^2\phi_j + 1]^{1/2}}, \tag{2b}$$

$$\frac{P_j}{P_i} = H(\gamma, M_i, \phi_j) = \frac{1}{\gamma+1}[2\gamma M_i^2\sin^2\phi_j - (\gamma-1)], \tag{2c}$$

and

$$\frac{a_j}{a_i} = W(\gamma, M_i, \phi_j) = \frac{[(\gamma-1)M_i^2\sin^2\phi_j + 2]^{1/2}[2\gamma M_i^2\sin^2\phi_j - (\gamma-1)]^{1/2}}{(\gamma+1)M_i\sin\phi_j}, \tag{2d}$$

where $M = u/a$ is the flow Mach number and a is the local speed of sound.

In the following, analytical models for solving the wave configurations associated with both regular and irregular S-O-S interactions are developed. The solution is constructed by formulating the appropriate governing equations around points at which the various discontinuities intersect and applying, whenever necessary, appropriate matching conditions.

2.3. *Analytical solution of a regular S-O-S interaction*

2.3.1. *Solution of the bow shock wave*

The flow fields on both sides of the bow shock wave emanating from the leading edge of the wedge (see figures 3a and 3b) are described by the following equations which are simply obtained from (2a) to (2d):

$$\theta_w = F(\gamma, M_\infty, \beta), \quad M_1 = G(\gamma, M_\infty, \beta), \tag{3a, b}$$

$$P_1 = P_0 H(\gamma, M_\infty, \beta), \quad a_1 = a_0 W(\gamma, M_\infty, \beta), \tag{3c, d}$$

where M_∞ is the free-stream Mach number, β is the angle of incidence of the bow shock wave as shown in figure 3(a), and $\theta_w = \delta + \alpha$, where δ is the half-wedge angle and α is its angle of attack.

https://doi.org/10.1017/S0022112097005326 Published online by Cambridge University Press

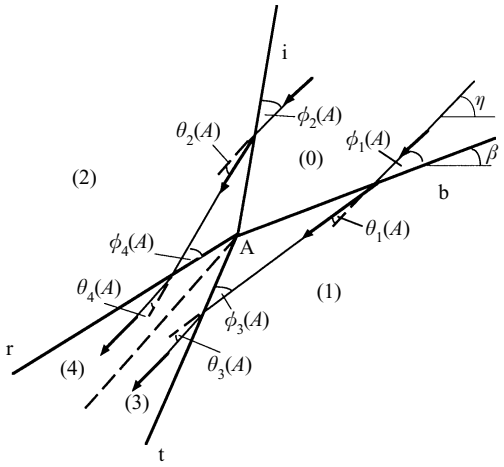


FIGURE 6. Definition of the parameters around point A of figures 3(*a*) and 3(*b*).

2.3.2. *Solution around point A* (*figure 3a or 3b*)

The flow field around point A at which the incident (impingement) and the bow (wedge) shock waves intersect is shown in figure 6, which, in fact, is a detailed enlargement of the appropriate parts in figures 3(*a*) and 3(*b*). Since the frame of reference is attached to point A, all the dynamic properties, which are frame-of-reference dependent are appropriately marked.

The velocity of point A to which the frame of reference is attached is

$$V_A = \frac{M_s + M_\infty \cos\lambda}{\cos(\beta+\lambda)} a_0, \tag{4}$$

where M_s is the impingement shock wave Mach number, λ is its angle of propagation with respect to the horizontal direction (see figure 2). Note here that λ is an algebraic quantity and is positive as shown in figure 3. In the frame of reference attached to point A the flow parameters in region (0) can be expressed as

$$M_0(A) = \left[\left(\frac{V_A}{a_0}\right)^2 + M_\infty^2 - 2\frac{V_A}{a_0} M_\infty \cos\beta\right]^{1/2}, \tag{5}$$

$$\eta = \arctan\left(\frac{V_A \sin\beta}{V_A \cos\beta - M_\infty a_0}\right), \tag{6}$$

$$\phi_1(A) = \eta - \beta, \tag{7}$$

$$\phi_2(A) = \tfrac{1}{2}\pi - \lambda - \eta. \tag{8}$$

By applying the oblique shock wave relations, one simply obtains

$$\theta_k(A) = F[\gamma, M_j(A), \phi_k(A)], \tag{9a–d}$$

$$M_k(A) = G[\gamma, M_j(A), \phi_k(A)], \tag{10a–d}$$

$$P_k(A) = P_j(A)\, H[\gamma, M_j(A), \phi_k(A)], \tag{11a–d}$$

$$a_k(A) = a_j(A)\, W[\gamma, M_j(A), \phi_k(A)], \tag{12a–d}$$

https://doi.org/10.1017/S0022112097005326 Published online by Cambridge University Press

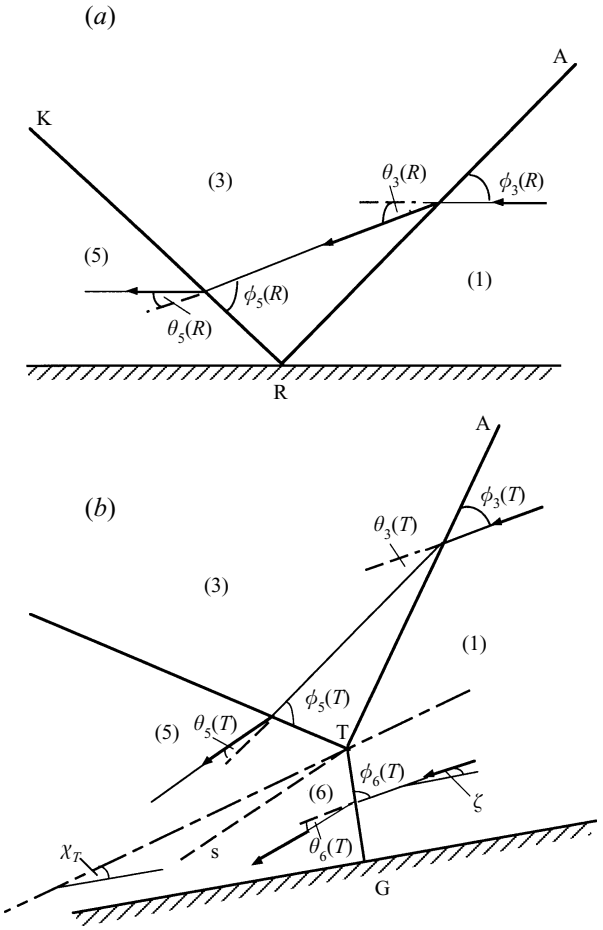


FIGURE 7. Definition of the parameters around (*a*) point R of the regular reflection shown in figure 3(*a*) and (*b*) point T of the Mach reflection shown in figure 3(*b*).

where $j = 0$ and $k = 2$ for the incident (impingement) shock wave (i), $j = 0$ and $k = 1$ for the original bow (wedge) shock wave (b), $j = 2$ and $k = 4$ for the refracted shock wave (r), $j = 1$ and $k = 3$ for the transmitted shock wave (t).

The matching conditions across the slipstream separating regions (3) and (4) are

$$\theta_3(A) - \theta_1(A) = \theta_2(A) - \theta_4(A), \tag{13}$$

$$P_3(A) = P_4(A). \tag{14}$$

Equations (4)–(14) consist of 23 equations and the following 23 unknowns: V_A, η, $\phi_1(A)$, $\phi_2(A)$, $\phi_3(A)$, $\phi_4(A)$, $\theta_1(A)$, $\theta_2(A)$, $\theta_3(A)$, $\theta_4(A)$, $M_0(A)$, $M_1(A)$, $M_2(A)$, $M_3(A)$, $M_4(A)$, $P_1(A)$, $P_2(A)$, $P_3(A)$, $P_4(A)$, $a_1(A)$, $a_2(A)$, $a_3(A)$ and $a_4(A)$. Consequently, the set is complete and solvable provided M_∞, λ, a_0 and P_0 are known, as indeed is the case.

As mentioned in the Introduction the transmitted shock wave (t) can reflect at the wedge surface either as a regular reflection (RR) or as a Mach reflection (MR). Detailed descriptions of the flow fields associated with these regular and Mach reflections are shown in figures 7(*a*) and 7(*b*), respectively. The frame of reference is attached to the reflection point, R, when solving the RR and to the triple point, T, when solving the MR.

https://doi.org/10.1017/S0022112097005326 Published online by Cambridge University Press

2.3.3. *Solution of the case with a regular reflection*

Since the frame of reference is attached to the reflection point R, the flow properties in region (1) which have already been solved in a frame of reference attached to point A must be first transformed with the aid of the following relations:

$$\phi_3(R) = \phi_3(A) + \phi_1(A) - \theta_1(A) + \beta - \theta_w, \tag{15}$$

$$M_1(R) = M_1(A) \sin \phi_3(A)/(\sin \phi_3(R)), \tag{16}$$

$$P_1(R) = P_1(A), \tag{17}$$

$$a_1(R) = a_1(A). \tag{18}$$

The oblique shock relations result in

$$\theta_k(R) = F[\gamma, M_j(R), \phi_k(R)], \tag{19a, b}$$

$$M_k(R) = G[\gamma, M_j(R), \phi_k(R)], \tag{20a, b}$$

$$P_k(R) = P_j(R)\, H[\gamma, M_j(R), \phi_k(R)], \tag{21a, b}$$

$$a_k(R) = a_j(R)\, W[\gamma, M_j(R), \phi_k(R)], \tag{22a, b}$$

where $k = 3$ and $j = 1$ for the shock wave AR, $k = 5$ and $j = 3$ for the shock wave KR.

The boundary condition of the regular reflection implies that

$$\theta_3(R) - \theta_5(R) = 0. \tag{23}$$

The set of equations (19)–(23) consists of nine equations and nine unknowns, namely $\theta_3(R)$, $\theta_5(R)$, $M_3(R)$, $M_5(R)$, $P_3(R)$, $P_5(R)$, $a_3(R)$, $a_5(R)$, and $\phi_5(R)$. Consequently, the set is complete and solvable in principle.

2.3.4. *Solution of the case with a Mach reflection*

Since the frame of reference is attached to the triple point T, the flow properties in region (1) which have already been solved in a frame of reference attached to point A must first be transformed. The velocity of the triple point T in the laboratory frame of reference is

$$V_T = \frac{M_1(A) \sin \phi_3(A) + M_1 \sin [\eta + \phi_3(A) - \theta_1(A) - \theta_w]}{\sin [\eta + \phi_3(A) - \theta_1(A) - \theta_w - \chi_T]} a_1, \tag{24a}$$

where, χ_T, the triple-point trajectory angle, is the angle between the wedge surface and the trajectory of the triple point T.

The angle $\phi_3(T)$ can be obtained from

$$\phi_3(T) = \eta + \phi_3(A) - \theta_1(A) - \theta_w - \zeta, \tag{24b}$$

where

$$\zeta = \arctan\left(\frac{V_T \sin \chi_T}{V_T \cos \chi_T - M_1 a_1}\right). \tag{24c}$$

In the above equations, M_1 and a_1 are the Mach number and the speed of sound of the flow in region (1) in the laboratory frame of reference, respectively. Note that they have already been calculated by (3*b*) and (3*d*).

The above-mentioned transformation is performed with the aid of the following relations:

$$M_1(T) = M_1(A) \sin \phi_3(A)/(\sin \phi_3(T)), \tag{25}$$

$$P_1(T) = P_1(A), \tag{26}$$

$$a_1(T) = a_1(A). \tag{27}$$

https://doi.org/10.1017/S0022112097005326 Published online by Cambridge University Press

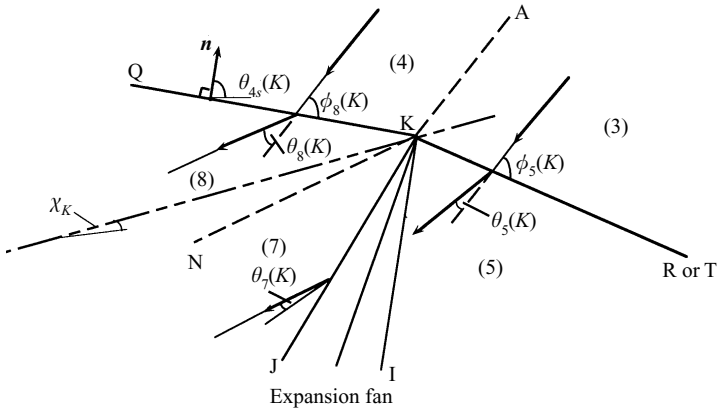


FIGURE 8. Definition of the parameters around point K of figures 3(*a*) and 3(*b*).

The oblique shock wave relations result in

$$\theta_k(T) = F[\gamma, M_j(T), \phi_k(T)], \tag{28a–c}$$

$$M_k(T) = G[\gamma, M_j(T), \phi_k(T)], \tag{29a–c}$$

$$P_k(T) = P_j(T)\, H[\gamma, M_j(T), \phi_k(T)], \tag{30a–c}$$

$$a_k(T) = a_j(T)\, W[\gamma, M_j(T), \phi_k(T)], \tag{31a–c}$$

where $k = 3$ and $j = 1$ for the shock wave AT, $k = 5$ and $j = 3$ for the shock wave KT, $k = 6$ and $j = 1$ for the shock wave TG (i.e. the Mach stem of the MR).

The matching conditions across the slipstream are

$$P_5(T) = P_6(T), \tag{32}$$

$$\theta_3(T) - \theta_5(T) = \theta_6(T). \tag{33}$$

Assuming that the Mach stem, TG, is straight and perpendicular to the wedge surface results in

$$\phi_6(T) = \tfrac{1}{2}\pi - \zeta. \tag{34}$$

Equations (25)–(34) consist of 21 equations and 21 unknowns. The unknowns are V_T, ζ, $\theta_3(T)$, $\theta_5(T)$, $\theta_6(T)$, $M_1(T)$, $M_3(T)$, $M_5(T)$, $M_6(T)$, $P_1(T)$, $P_3(T)$, $P_5(T)$, $P_6(T)$, $a_1(T)$, $a_3(T)$, $a_5(T)$, $a_6(T)$, $\phi_3(T)$, $\phi_5(T)$, $\phi_6(T)$ and χ_T. Consequently, the set of equations is complete and solvable in principle.

2.3.5. *Solution around point K* (*figure 3a or 3b*)

As shown in figures 3(*a*) and 3(*b*), the reflected shock wave of either the RR or the MR intersects the slipstream emanating from point A at point K. The resulting wave configuration is shown in figure 8. The velocity of point A in a frame of reference attached to point K, $V_A(K)$, can be obtained from the following relations:

$$|V_A(K)| = |V_A - V_K| = \frac{\overline{OA} - \overline{OK}}{\Delta t} = \frac{\overline{AK}}{\Delta t}, \tag{35}$$

where V_A and V_K are the velocity vectors of points A and K in a laboratory frame of reference, and $\Delta t = \overline{OA}/V_A$, is the time elapsed since the S-O-S interaction started.

https://doi.org/10.1017/S0022112097005326 Published online by Cambridge University Press

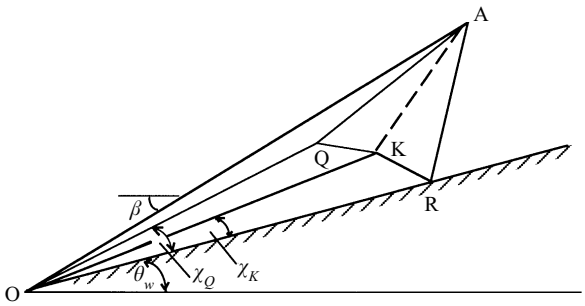


FIGURE 9. Geometrical relations between points O, A, R, K and Q of figure 3(*a*).

Applying the sine-law for the triangle AOK (figure 9) and combining with equation (34) results in

$$V_A(K) = |V_A(K)| = \frac{V_A \sin(\beta - \theta_w - \chi_K)}{\sin[\phi_1(A) + \theta_3(A) + \beta - \theta_1(A) - \theta_w - \chi_K]}. \tag{36}$$

Since the solution of the flow field around point K is done in a frame of reference attached to it, the flow properties in regions (3) and (4), which have already been solved in previous stages, must be transformed appropriately. This transformation is performed with the aid of the following expressions:

$$M_3(K) = M_3(A) - V_A(K)/a_3(K), \quad M_4(K) = M_4(A) - V_A(K)/a_4(K), \tag{37a, b}$$

$$a_3(K) = a_3(A), \quad a_4(K) = a_4(A), \tag{37c, d}$$

$$P_3(K) = P_3(A), \quad P_4(K) = P_4(A). \tag{37e, f}$$

$\phi_5(K)$ can be obtained using geometrical relations of the triangle ARK (figure 3*a*) or of the triangle ATK (figure 3*b*). In the following only the equations associated with the RR (figure 3*a*) are derived, since those associated with the MR (figure 3*b*) are similar. An inspection of the triangle ARK (see figure 9) together with figures 6 and 7 implies that

$$\phi_5(K) = \phi_5(R) + \phi_3(R) + \theta_3(A) - \phi_3(A) - \theta_3(R). \tag{38}$$

The trajectory angle of point K, χ_K, can be obtained by applying the sine law to three triangles, OAR, PKR and AKR, as shown in figure 9, which results in

$$\frac{\sin\chi_K \sin[\phi_3(A) - \theta_1(A) + \eta - \beta]}{\sin[\chi_K + \phi_5(R) - \theta_5(R)]} = \frac{\sin(\beta - \theta_w)\sin[\phi_3(A) - \theta_3(A)]}{\sin[\phi_5(R) + \phi_3(R) + \theta_3(A) - \phi_3(A) - \theta_3(R)]}. \tag{39}$$

Now we are at the stage of solving the flow field around point K which, as shown in figure 8, consists of two shock waves, KR (or KT) and KQ, two slipstreams, KA and KN, and one centred expansion fan. The flow field across the two oblique shock waves can be obtained with the aid of the general oblique shock relation

$$\theta_i(K) = F[\gamma, M_j(K), \phi_i(K)], \tag{40a, b}$$

$$M_i(K) = G[\gamma, M_j(K), \phi_i(K)], \tag{41a, b}$$

$$P_i(K) = P_j(K)\, H[\gamma, M_j(K), \phi_i(K)], \tag{42a, b}$$

$$a_i(K) = a_j(K)\, W[\gamma, M_j(K), \phi_i(K)], \tag{43a, b}$$

where $i = 5$ and $j = 3$ for the shock wave KR, $i = 8$ and $j = 4$ for the shock wave KQ.

https://doi.org/10.1017/S0022112097005326 Published online by Cambridge University Press

The relations across the centred expansion fan which connects regions (5) and (7) are

$$\nu[M_7(K)] = \nu[M_5(K)] + \theta_7(K), \tag{44}$$

$$P_7(K) = P_5(K)\left[\frac{1+\frac{1}{2}(\gamma-1)\,M_5^2(K)}{1+\frac{1}{2}(\gamma-1)\,M_7^2(K)}\right]^{\gamma/(\gamma-1)}, \tag{45}$$

$$a_7(K) = a_5(K)\left[\frac{1+\frac{1}{2}(\gamma-1)\,M_5^2(K)}{1+\frac{1}{2}(\gamma-1)\,M_7^2(K)}\right]^{1/2}, \tag{46}$$

where the Prandtl–Meyer function $\nu(M)$ is defined as follows:

$$\nu(M) = \left(\frac{\gamma+1}{\gamma-1}\right)^{1/2}\arctan\left[\frac{\gamma-1}{\gamma+1}(M^2-1)\right]^{1/2} - \arctan\,(M^2-1)^{1/2}.$$

The matching conditions across the slipstream, KN, are

$$P_7(K) = P_8(K), \tag{47}$$

$$\theta_5(K) + \theta_7(K) = \theta_8(K). \tag{48}$$

The set of equations (40)–(48) is complete and solvable since it consists of 13 equations and 13 unknowns, namely $\theta_5(K)$, $\theta_7(K)$, $\theta_8(K)$, $M_5(K)$, $M_7(K)$, $M_8(K)$, $a_5(K)$, $a_7(K)$, $a_8(K)$, $P_5(K)$, $P_7(K)$, $P_8(K)$ and χ_K.

2.3.6. *Solution around point Q* (*figure 3a or 3b*)

The velocity of point A in a frame of reference attached to point Q, i.e. $V_A(Q)$, can be expressed as (see figures 9 and 10)

$$V_A(Q)/\overline{AQ} = V_A/\overline{OA}. \tag{49}$$

Applying the sine law to triangle OAQ and combining with (49) yields

$$V_A(Q) = \frac{V_A\sin\,(\beta-\theta_w-\chi_Q)}{\sin\,[\beta-\theta_w-\chi_Q+\phi_1(A)-\theta_1(A)-\phi_4(A)+\theta_4(A)+\theta_3(A)]}. \tag{50}$$

The flow Mach number in region (2) relative to point Q can be found from figure 10(*a*) by applying the cosine law:

$$M_2(Q) = \left\{M_2^2(A) + \left[\frac{V_A(Q)}{a_2(Q)}\right]^2 - 2\frac{M_2(A)\,V_A(Q)}{a_2(Q)}\cos\,[\phi_4(A)]\right\}^{1/2}. \tag{51}$$

Applying the sine law and rearranging results in

$$\phi_4(Q) = \phi_4(A) + \arcsin\left[\frac{M_2(Q)\,a_2(Q)}{V_A(Q)}\sin\,\phi_4(A)\right], \tag{52}$$

where $a_2(Q) = a_2(A)$ and $P_2(Q) = P_2(A)$. The above equations are sufficient to obtain $M_2(Q)$ and $\phi_2(Q)$. By using the oblique shock relations one can get (see figure 10*b*)

$$\theta_k(Q) = F[\gamma, M_j(Q), \phi_k(Q)], \tag{53a–c}$$

$$M_k(Q) = G[\gamma, M_j(Q), \phi_k(Q)], \tag{54a–c}$$

$$P_k(Q) = P_j(Q)\,H[\gamma, M_j(Q), \phi_k(Q)], \tag{55a–c}$$

$$a_k(Q) = a_j(Q)\,W[\gamma, M_j(Q), \phi_k(Q)], \tag{56a–c}$$

where $k = 4$ and $j = 2$ for the shock wave QA, $k = 9$ and $j = 2$ for the shock wave QC, $k = 8$ and $j = 4$ for the shock wave QK.

https://doi.org/10.1017/S0022112097005326 Published online by Cambridge University Press

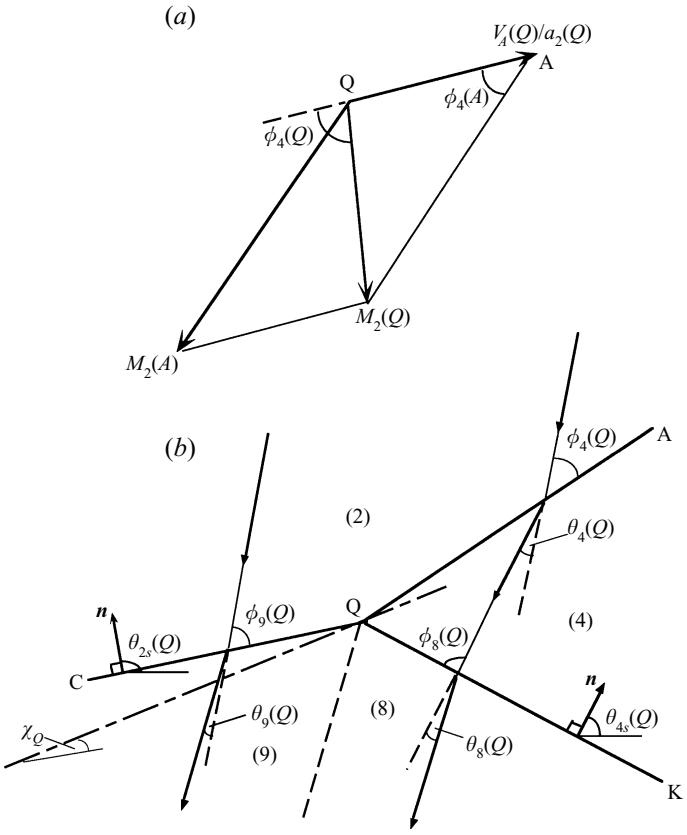


FIGURE 10. (*a*) The velocity vectors around point Q; (*b*) definition of the parameters around point Q of figures 3(*a*) and 3(*b*).

The matching conditions across the slipstream are

$$P_8(Q) = P_9(Q), \tag{57}$$

$$\theta_4(Q) - \theta_8(Q) = \theta_9(Q). \tag{58}$$

The set of equations (53) to (58) consists of 14 equations and 15 unknowns, that is $\theta_4(Q)$, $\theta_8(Q)$, $\theta_9(Q)$, $M_4(Q)$, $M_8(Q)$, $M_9(Q)$, $P_4(Q)$, $P_8(Q)$, $P_9(Q)$, $a_4(Q)$, $a_8(Q)$, $a_9(Q)$, $\phi_8(Q)$, $\phi_9(Q)$ and χ_Q. To complete this set of equations an additional equation is required.

The curved shock wave KQ is disturbed by the expansion waves reflected from the wedge surface. If one assumes that these expansion waves are simple waves then by using the geometrical shock dynamics theory (see Han & Yin 1993) one can get

$$\theta_{4s}(Q) - \theta_{4s}(K) = \int_{M_Q}^{M_k} \left[\frac{2}{(M^2-1)\,\Lambda(M)}\right]^{1/2} \mathrm{d}M, \tag{59a}$$

$$\Lambda(M) = \left[2(2\mu+1+M^{-2})^{-1}\left(1+\frac{2}{\gamma+1}\frac{1-\mu^2}{\mu}\right)^{-1}\right], \tag{59b}$$

and

$$\mu = \left[\frac{(\gamma-1)\,M^2+2}{2\gamma M^2-(\gamma-1)}\right]^{1/2}, \tag{59c}$$

https://doi.org/10.1017/S0022112097005326 Published online by Cambridge University Press

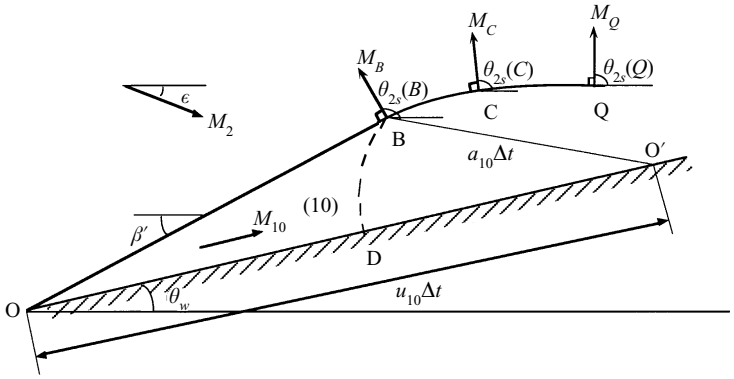


FIGURE 11. Schematic illustration of the new bow shock wave and definition of parameters.

where $\theta_{4s}(Q)$ and $\theta_{4s}(K)$ are the orientation angles of the curved shock KQ at points Q and K, respectively. M_K and M_Q are the strengths of the curved shock wave KQ at points K and Q, respectively, and $\Lambda(M)$ is a slowly varying function. $\Lambda(M) = 0.5$ for $M \to 1$ and $\Lambda(M) = 0.4$ for $M \to \infty$.

It is clearly evident from figure 10(*b*) that

$$M_K = M_4(K)\sin[\phi_8(K)], \quad M_Q = M_4(Q)\sin[\phi_8(Q)], \tag{59d, e}$$

$$\theta_{4s}(K) = \tfrac{1}{2}\pi + \beta + \phi_1(A) + \theta_3(A) - \theta_1(A) - \phi_8(K), \tag{59f}$$

$$\theta_{4s}(Q) = \beta + \phi_1(A) + \theta_4(A) + \theta_3(A) + \phi_4(Q) + \phi_8(Q) - \phi_4(A) - \theta_1(A) - \theta_4(Q) - \tfrac{1}{2}\pi. \tag{59g}$$

Since $(M_K - M_Q)/M_K \ll 1$, $\Lambda(M)$ can be regarded as a constant. Consequently, equation (59*a*) can be rewritten as

$$M_Q = \cosh\{\cosh^{-1}(M_K) + (\Lambda/2)^{1/2}[\theta_{4s}(K) - \theta_{4s}(Q)]\}. \tag{60}$$

Equation (60) completes the set of equations (53)–(58) which as noted earlier lacked one equation compared to the number of its unknowns.

2.3.7. *Solution of the new bow shock*

The new bow shock results from the interaction of the incident (impingement) shock-induced flow with the wedge. As shown in figure 2(*b*), the angle between the flow direction and the horizontal axis, ϵ, can be expressed as

$$\epsilon = \arctan\left\{\frac{M_2(A)\sin[\eta + \theta_2(A)] - (V_A/a_2)\sin\beta}{(V_A/a_2)\cos\beta - M_2(A)\cos[\eta + \theta_2(A)]}\right\}. \tag{61}$$

Similarly, the induced-flow Mach number in a laboratory frame of reference, M_2, is

$$M_2 = \{M_2^2(A) + (V_A/a_2)^2 - 2M_2(A)(V_A/a_2)\cos[\phi_1(A) + \theta_2(A)]\}^{1/2}. \tag{62}$$

Applying the oblique shock relations results in

$$\theta_w + \epsilon = F(\gamma, M_2, \beta' + \epsilon), \tag{63}$$

$$M_{10} = G(\gamma, M_2, \beta' + \epsilon), \tag{64}$$

$$a_{10} = a_2 H(\gamma, M_2, \beta' + \epsilon), \tag{65}$$

$$P_{10} = P_2 W(\gamma, M_2, \beta' + \epsilon), \tag{66}$$

where as shown in figure 11, β' is the angle of incidence of the new bow shock. As

https://doi.org/10.1017/S0022112097005326 Published online by Cambridge University Press

shown in figure 3(*a*) the straight new bow shock interacts with the shock wave issuing from point Q. The interaction results in a curved portion of bow shock, BQ.

Similar to the analysis of Li, Ben-Dor & Han (1994), two families of disturbances propagate along the shock BQ. One starts at B and the other starts at Q. Let us assume that these disturbances cannot cross each other and that they meet at point C. From a shock dynamics point of view, the shock waves BC and QC are disturbed by simple waves. By using the shock-expansion relations one can get

$$\theta_{2s}(Q)-\theta_{2s}(C)=\int_{M_Q}^{M_C}\left[\frac{2}{(M^2-1)\,A(M)}\right]^{1/2}\mathrm{d}M, \tag{67}$$

$$\theta_{2s}(B)-\theta_{2s}(C)=\int_{M_C}^{M_B}\left[\frac{2}{(M^2-1)\,A(M)}\right]^{1/2}\mathrm{d}M, \tag{68}$$

where as shown in figure 11, $\theta_{2s}(Q)$, $\theta_{2s}(C)$ and $\theta_{2s}(B)$ are the shock orientations at points Q, C and B, respectively, and M_Q, M_C and M_B, are the strengths of the shock waves at points Q, C and B, respectively. In addition,

$$M_Q=M_2(Q)\sin\phi_9(Q),\quad M_B=M_2\sin(\beta'+\epsilon), \tag{69a, b}$$

$$\theta_{2s}(Q)=\tfrac{1}{2}\pi+\beta+\phi_4(Q)+\phi_1(A)+\theta_4(A)+\theta_3(A)-\theta_1(A)-\phi_4(A)-\phi_9(Q), \tag{69c}$$

$$\theta_{2s}(Q)=\tfrac{1}{2}\pi+\beta'. \tag{69d}$$

The locations of points B and D are

$$\frac{\overline{OB}}{\overline{OA}}=\frac{a_{10}}{V_A}\{M_{10}\cos(\beta'-\theta_w)-[1-M_{10}^2\sin^2(\beta'-\theta_w)]^{1/2}\}, \tag{70a}$$

$$\frac{\overline{OD}}{\overline{OR}}=\frac{a_{10}\sin[\phi_3(A)-\theta_1(A)+\eta-\theta_w]}{V_A\sin[\phi_3(A)-\theta_1(A)+\eta-\beta]}. \tag{70b}$$

The shape of the curved shock wave BCQ can be expressed as two second-order polynomials which match at point C. Since the derivation is similar to that done by Li *et al*. (1994), only the final results are given subsequently.

2.4. *Analytical solution of an irregular S-O-S interaction*

The irregular S-O-S interaction wave configuration is shown in figure 4. The incident (impingement) shock interacts with the bow shock, which produces a Mach stem EF. The points E and F can be regarded as two triple points.

2.4.1. *Solution around points E and F*

The velocity of point E in a laboratory frame of reference is

$$V_E=\frac{M_s+M_\infty\cos\lambda}{\cos(\chi_E+\theta_w+\lambda)}a_0, \tag{71}$$

where χ_E, as shown in figure 4, is the trajectory angle of point E. Note that λ is negative in figure 4.

In a frame of reference attached to point E (see figure 12) the flow parameters in region (0) can be obtained using the following relations:

$$M_0(E)=[(V_E/a_0)^2+M_\infty^2-2(V_E/a_0)\,M_\infty\cos(\chi_E+\theta_w)]^{1/2}, \tag{72}$$

$$\phi_2(E)=\tfrac{1}{2}\pi-\xi-\lambda, \tag{73}$$

https://doi.org/10.1017/S0022112097005326 Published online by Cambridge University Press

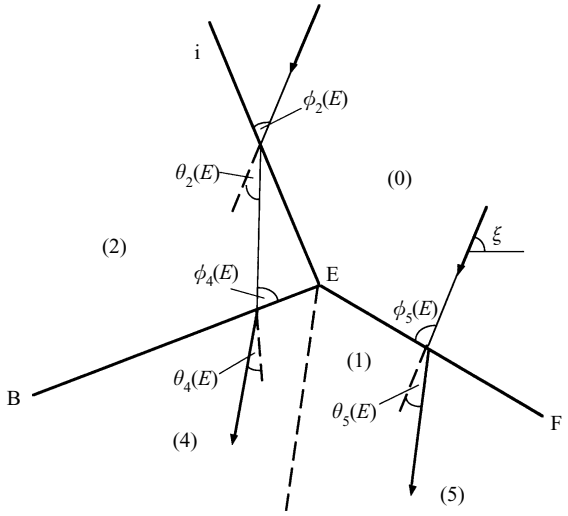


FIGURE 12. Definition of the parameters around point E for the irregular S-O-S interaction shown in figure 4.

and
$$\xi = \arctan\left[\frac{V_E \sin(\chi_E + \theta_w)}{V_E \cos(\chi_E + \theta_w) - M_\infty a_0}\right]. \tag{74}$$

Applying the oblique shock wave relations to the shock waves shown in figure 12 results in

$$\theta_k(E) = F\{\gamma, M_j(E), \phi_k(E)\}, \tag{75a–c}$$

$$M_k(E) = G[\gamma, M_j(E), \phi_k(E)], \tag{76a–c}$$

$$P_k(E) = P_j(E)\, H[\gamma, M_j(E), \phi_k(E)], \tag{77a–c}$$

$$a_k(E) = a_j(E)\, W[\gamma, M_j(E), \phi_k(E)], \tag{78a–c}$$

where $j = 0$ and $k = 2$ for the incident (impingement) shock wave (i), $j = 0$ and $k = 5$ for the shock wave (m), $j = 2$ and $k = 4$ for the shock wave (r′).

The matching conditions across the slipstream are

$$P_4(E) = P_5(E), \tag{79}$$

$$\theta_2(E) - \theta_4(E) = \theta_5(E). \tag{80}$$

Equations (71)–(80) consist of 18 equations with 19 unknowns, i.e. V_E, $\theta_2(E)$, $\theta_4(E)$, $\theta_5(E)$, $M_0(E)$, $M_2(E)$, $M_4(E)$, $M_5(E)$, $P_2(E)$, $P_4(E)$, $P_5(E)$, $\phi_2(E)$, $\phi_4(E)$, $\phi_5(E)$, $a_2(E)$, $a_4(E)$, $a_5(E)$, $\chi(E)$ and ξ. Therefore, an additional equation is needed to complete this set. Experimental photographs indicate that the Mach stem EF is short and only slightly curved. Consequently the assumption that the Mach stem is straight seems to be reasonable.

If the shock wave EF is assumed to be straight, the velocity of point F in a laboratory frame of reference (see figure 4), V_F, can be easily found by applying the sine law to the triangle OEF, i.e.

$$V_F = V_E \frac{\overline{OF}}{\overline{OE}} = V_E \frac{\sin(\angle OEF)}{\sin(\angle OFE)} = V_E \frac{\sin[\xi + \phi_5(E) - \chi_E - \theta_w]}{\sin[\phi_5(E) + \xi - \beta]}. \tag{81}$$

https://doi.org/10.1017/S0022112097005326 Published online by Cambridge University Press

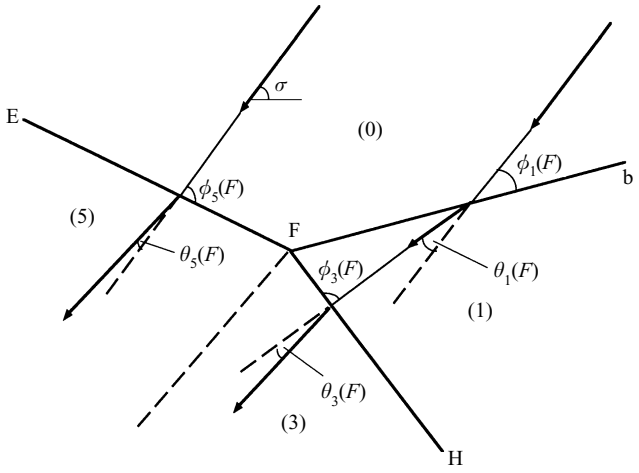


FIGURE 13. Definition of parameters around point F for the irregular S-O-S interaction shown in figure 4.

The flow parameters in region (0) in a frame of reference attached to point F (see figure 13) can be obtained using the following expressions:

$$M_0(F) = [(V_F/a_0)^2 + M_\infty^2 - 2(V_F/a_0)\, M_\infty \cos\beta]^{1/2}, \tag{82a}$$

$$\phi_5(F) = \sigma + \pi - \phi_5(E) - \xi, \tag{82b}$$

$$\phi_1(F) = \sigma - \beta, \tag{81c}$$

and

$$\sigma = \arctan\left[\frac{V_F \sin\beta}{V_F \cos\beta - M_\infty\, a_0}\right]. \tag{82d}$$

Applying the oblique shock wave relations to the oblique shock waves shown in figure 13 results in

$$\theta_k(F) = F[\gamma, M_j(F), \phi_k(F)], \tag{83a–c}$$

$$M_k(F) = G[\gamma, M_j(F), \phi_k(F)], \tag{84a–c}$$

$$P_k(F) = P_j(F)\, H[\gamma, M_j(F), \phi_k(F)], \tag{85a–c}$$

$$a_k(F) = a_j(F)\, W[\gamma, M_j(F), \phi_k(F)], \tag{86a–c}$$

where $j = 0$ and $k = 1$ for the bow shock wave (b), $j = 0$ and $k = 5$ for the shock wave (m), $j = 1$ and $k = 3$ for the shock wave (t).

The matching conditions across the slipstream are

$$P_3(F) = P_5(F), \tag{87}$$

$$\theta_1(F) - \theta_3(F) = \theta_5(F). \tag{88}$$

Equations (81)–(88) consist of 19 equations with 18 unknowns, i.e. V_F, $\theta_1(F)$, $\theta_3(F)$, $\theta_5(F)$, $M_0(F)$, $M_1(F)$, $M_3(F)$, $M_5(F)$, $P_1(F)$, $P_3(F)$, $P_5(F)$, $a_1(F)$, $a_3(F)$, $a_5(F)$, $\phi_1(F)$, $\phi_3(F)$, $\phi_5(F)$ and σ. By combining the two sets of equations (75)–(80) which has one extra unknown and (81)–(88) which lacks one unknown, one obtains a new combined set, which consists 37 equations with 37 unknowns. The solution of this set provides, simultaneously, the solutions of the flow fields around points E and F.

2.4.2. *Shapes of the new bow shock and the transmitted shock*

The shape of the new bow shock can be obtained by using the method outlined earlier for calculating the shape of the shock wave KQ (see figure 3*b*). Consequently, in the following only the shape of the transmitted shock FH (see figure 4) is dealt with.

https://doi.org/10.1017/S0022112097005326 Published online by Cambridge University Press

If one assumes that only simple waves propagate along the transmitted shock, FH, and cause it to curve, then the following relations which arise from the shock dynamics theory are self-explanatory:

$$\theta_H - \theta_F = \int_{M_H}^{M_F} \left[\frac{2}{(M^2-1)\,\Lambda(M)}\right]^{1/2} \mathrm{d}M, \tag{89}$$

where θ_F and θ_H are the shock wave orientation angles at points F and H, respectively, and M_F and M_H are the strengths of the shock wave at points F and H, respectively. Since the shock wave FH is perpendicular to the wedge surface at point H,

$$\theta_H = \theta_w, \tag{90}$$

$$\theta_F = \phi_1(F) + \phi_3(F) + \beta - \theta_1(F) - \tfrac{1}{2}\pi, \tag{91}$$

and

$$M_F = M_1(F)\sin\phi_3(F). \tag{92}$$

Thus, M_H can be obtained from

$$M_H = \cosh\{\cosh^{-1}[M_1(F)\sin\phi_3(F)] + \tfrac{1}{4}\Lambda^{1/2}[\tfrac{1}{2}\pi + \theta_1(F) + \theta_w - \phi_1(F) - \phi_3(F) - \beta]\} \tag{93}$$

under the assumption that $(M_F - M_H)/M_F \ll 1$. The length of OH can be calculated from

$$\overline{OH} = \overline{OF}\, M_H\, a_1/V_F. \tag{94}$$

Assuming that the shape of the shock wave FH can be expressed by a third-order polynomial, e.g.

$$x - x_H = a(y-y_H)^2 + b(y-y_H)^3, \tag{95a}$$

where $x_H = \overline{OH}$ and $y_H = 0$. The coordinates of point F (x_F, y_F) and the slope of the curve at point F are

$$x_F = \overline{OF}\cos(\beta - \theta_w), \quad y_F = \overline{OF}\sin(\beta - \theta_w), \tag{95b, c}$$

and

$$\mathrm{d}x/\mathrm{d}y|_F = \tan(\theta_H - \theta_F). \tag{95d}$$

Consequently, the expression for the shape of the shock wave FH is

$$x = x_H + \frac{(y-y_H)^2}{y_F^2}[x_F - x_H - 2y_F\tan(\theta_H - \theta_F)] + \frac{(y-y_H)^3}{y_F^3}[y_F + \tan(\theta_H - \theta_F) - 2(x_F - x_H)]. \tag{96}$$

The shape of the new bow shock can be solved in a way similar to that for a regular S-O-S interaction, shown earlier.

3. Results and discussion

The model equations, derived in §2, were solved by MATLAB. Since the equations comprising each set did not have to be solved simultaneously, a step-by-step solution procedure was applied. Using this procedure the entire set of equations could be subdivided into smaller sets which sometimes even consisted of only one equation, e.g. equation (4) is independent of the rest of the equations in the set of 23 equations given by (4)–(14). In addition, the solution of some sets of equations require initial guesses of the unknowns. It was found that the most sensitive ones were the angles while the

https://doi.org/10.1017/S0022112097005326 Published online by Cambridge University Press

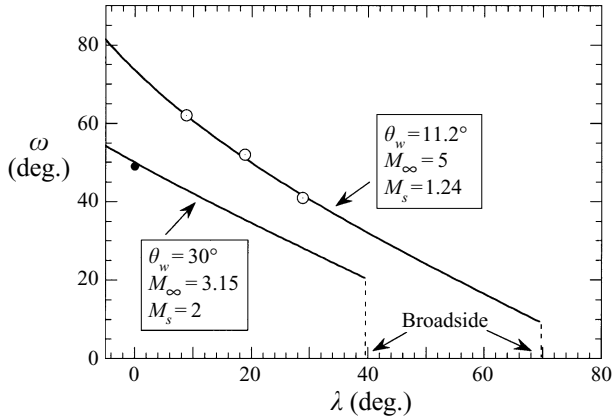


FIGURE 14. Dependence of the transmitted shock wave angle, ω, on λ. Open and solid circles are numerical results of Kutler *et al.* (1975) for two seats of parameters, respectively.

flow parameters (e.g. Mach number, pressure, density, etc.) were not too sensitive. Whenever a solution converged to an aphysical solution the initial guesses for the angles were changed and the solution process was repeated. In all the calculations, the specific heat capacities ratio was $\gamma = 1.4$.

In order to check the accuracy of the model developed here, the predicted values of the transmitted shock wave angle, ω (see figure 3*a*), $\omega = \phi_3(A) + \phi_1(A) - \theta_1(A) + \beta - \theta_w$, which is considered to be essential for the subsequent analysis, were compared with Kutler *et al.*'s (1975) numerical results. For the two cases shown in figure 14, the agreement between the analytical and the numerical predictions is excellent. It should be noted here that the 'broadside' shown in figure 14 is now defined as $\lambda = \frac{1}{2}\pi - \beta$, rather than $\lambda = \frac{1}{2}\pi - \theta_w$ as defined by Kutler *et al.* (1975), because when $\lambda > \frac{1}{2}\pi - \beta$, the impingement shock wave (i) cannot begin to interact with the bow shock wave (b) at the leading edge of the wedge.

As mentioned earlier, the transmitted shock wave (t) reflects over the wedge surface as either a regular reflection (RR) or a Mach reflection (MR). When its strength and orientation are known, the RR $\leftrightarrow$ MR transition criterion can be obtained by combining (19)–(23) with the following equation:

$$\sin_2 \phi_5(R) = \frac{1}{\gamma M_3^2(R)} \{\tfrac{1}{4}(\gamma+1)\, M_3^2(R) - 1 + [(\gamma+1)\,(1+\tfrac{1}{2}(\gamma-1)\, M_3^2(R) + \tfrac{1}{16}(\gamma+1)\, M_3^4(R))]^{1/2}\} \tag{97}$$

which was derived from von Neumann's (1943) *detachment criterion*. Note that in the present case, the flow field ahead of the shock pattern is not at rest. This differs from pseudosteady shock wave reflections in shock tubes where the flow ahead of the shock wave is quiescent. The transition criterion for $\theta_w = 11.2°$, $M_\infty = 5$ and $\theta_w = 30°$, $M_\infty = 3.15$ in the (λ_{tr}, M_s)-plane is shown in figure 15. Kutler *et al.* (1975) found numerically that for $\theta_w = 11.2°$, $M_\infty = 5$ and $M_s = 1.24$, the RR $\leftrightarrow$ MR transition takes place at $\lambda_{tr} = 21.67°$, while the present predicted value is $\lambda_{tr} = 22.59°$. For the second case, $\theta_w = 30°$, $M_\infty = 3.15$, $M_s = 2$ and $\lambda = 0$, Kutler *et al.* (1975) obtained a RR wave configuration while Merritt & Aronson's (1967) experiment and the present prediction indicates a MR wave configuration, although the values of the transmitted shock angle, ω, were very close, i.e. $\omega = 49 \pm 1°$ in the experiment, $50 \pm 1°$ in the numerical calculation and 49.95° in the present analytical prediction. The disagreement between

https://doi.org/10.1017/S0022112097005326 Published online by Cambridge University Press

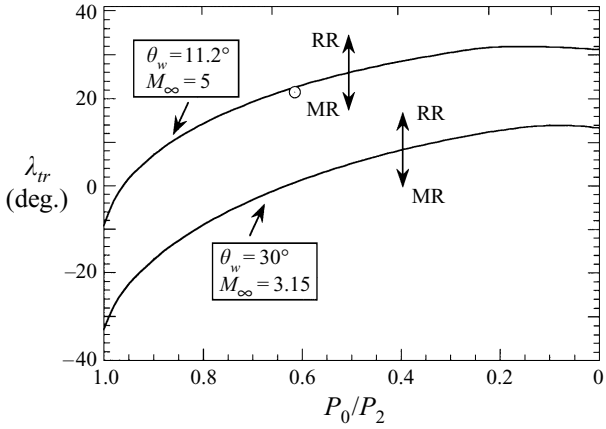


FIGURE 15. Dependence of the RR↔MR transition angle, λ_{tr}, on the strength of the impingement shock wave, P_0/P_2 or M_s. The open circle is a numerical result of Kutler *et al.* (1975).

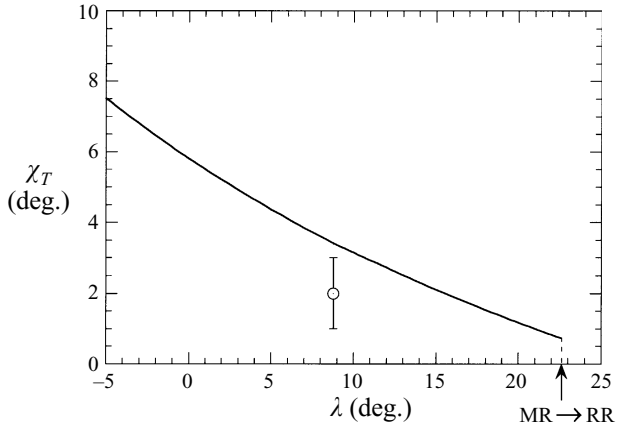


FIGURE 16. Dependence of the triple-point trajectory angle, χ_T, on λ for $\theta_w = 11.2°$, $M_\infty = 5$, $M_s = 1.24$. The open circle is a numerical result of Kutler *et al.* (1975).

the numerical simulation and the experiment was explained by Kutler *et al.* (1975) as a result of the shock wave/boundary interaction. This explanation is questionable since as shown by Ben-Dor (1991), the viscosity only marginally influences the transition angle. Note that the present predicted RR↔MR transition for the above listed conditions occurs at $\lambda_{tr} = 12.37°$. Consequently, since the difference between $\lambda = 0$ and $\lambda_{tr} = 12.37°$ is clearly not marginal, the difference in the overall phenomenon cannot be attributed to the neglect of viscous effects.

The prediction of the triple-point trajectory angle, χ_T, is essential for the study of Mach reflection wave configurations. The dependence of χ_T on λ is shown in figure 16, which indicates that χ_T decreases as λ increases. Note that the transition is reached at a point where χ_T is not equal to zero. This is consistent with the results for pseudosteady shock wave reflections in quiescent gas.

It is interesting to compare the triple-point trajectory angle of a Mach reflection between the cases in which the gas ahead of the wave configuration is quiescent and non-quiescent (the present case), for an identical shock wave strength and incident

https://doi.org/10.1017/S0022112097005326 Published online by Cambridge University Press

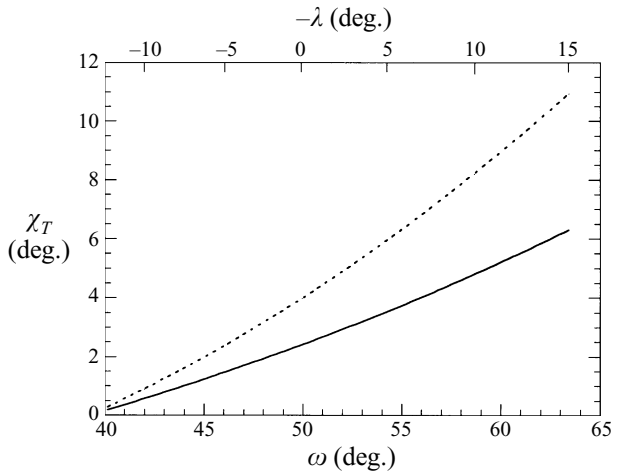


FIGURE 17. Dependence of the triple-point trajectory angle, χ_T, on the incident angle, ω for $\theta_w = 30°$, $M_\infty = 3.15$ and $M_s = 2$. Solid line – non-quiescent gas ahead of the shock pattern; dashed line – quiescent gas ahead of transmitted shock wave.

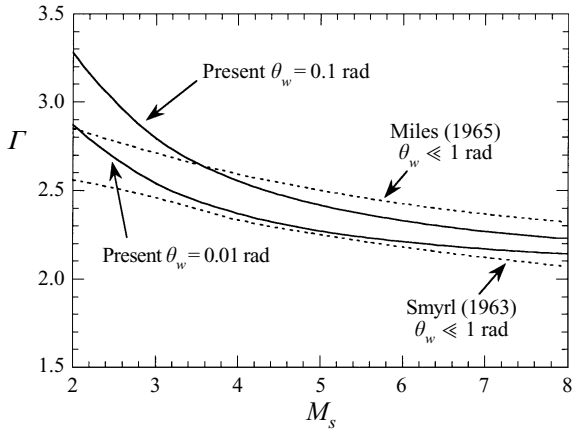


FIGURE 18. Comparisons of the present predicted normalized maximum surface pressure of the Mach reflections with Smyrl's (1963) and Miles' (1965) models.

angle. As shown in figure 17, χ_T for a quiescent gas (dashed line) is larger than for a non-quiescent gas (solid line). Similar results were obtained by Li & Ben-Dor (1995) when their shock–shock relations were applied to a non-quiescent gas.

The maximum pressure on the wedge surface is reached behind point R (region (5)) for RR (see figure 3*a*) and immediately behind the Mach stem (region (6)) for MR (see figure 3*b*). For a Mach reflection, Smyrl (1963) and Miles (1965) developed approximate methods, based on the perturbation theory and the geometric shock dynamics theory, respectively, to predict the wedge surface pressure behind the Mach stem. Their models were limited to very small wedge angles, i.e. $\theta_w \ll 1$ rad. The dependence of the predicted normalized maximum pressure, $\Gamma = (P_6 - P_2)/\gamma P_2 \theta_w$, on M_s is shown in figure 18. It was found that for $\theta_w = 0.1$ rad, $M_s \geqslant 3.5$ and $\theta_w = 0.01$ rad, $M_s \geqslant 2$, the values predicted by the present model are located between Smyrl's (1963) and Miles' (1965) results, who assumed $\theta_w \ll 1$ rad in their models.

https://doi.org/10.1017/S0022112097005326 Published online by Cambridge University Press

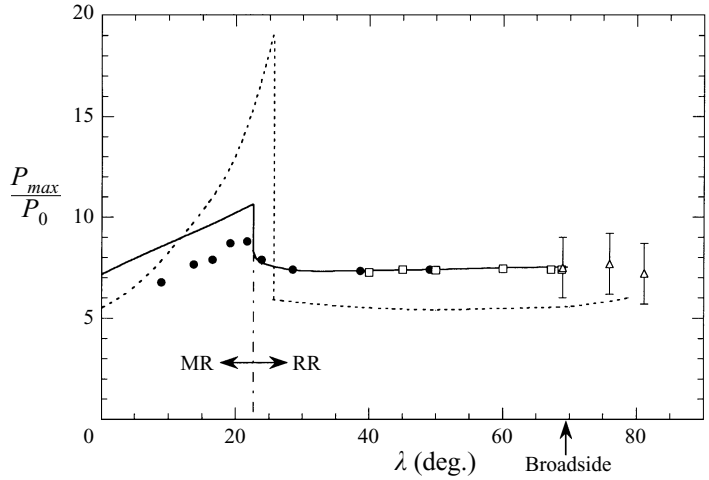


FIGURE 19. Dependence of the predicted maximum surface pressure P_{max}/P_0 on λ for both regular and Mach reflections for $\theta_w = 11.2°$, $M_\infty = 5$ and $M_s = 1.24$. Dashed line – approximate theory of Lagow & Murad (1975); solid circles – numerical results of Kutler *et al.* (1975); open triangles – experimental results of Ruetenik *et al.* (1973); open squares – characteristic method of Miller *et al.* (1964); solid line – present results.

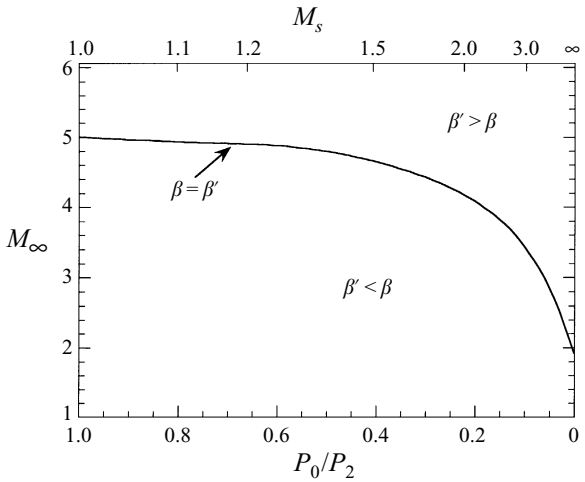


FIGURE 20. The relation between the original bow shock wave angle β and the new bow shock wave angle β' in the domain (M_∞, M_s) for a head-on interaction ($\lambda = 0$).

The dependence of the predicted maximum surface pressure P_{max}/P_0 on λ for both regular and Mach reflection wave configurations is shown in figure 19. For the RR case, the present prediction agrees well with the numerical (Kutler *et al.* 1975), the experimental (Ruetenik, Cole & Jones 1973) and the approximate theoretical (Miller, Schindel & Ruetenik 1964) results. For the MR case, the numerical predictions are smaller than the present analytical predictions. Since no experimental data are available to the authors, it is not clear which of these two predictions is closer to the actual values. Overall, the present analytical model is superior to the approximate theory (dashed line) developed by Lagow & Murad (1975). It is clear that P_{max}/P_0 jumps during the RR $\leftrightarrow$ MR transition. This is a well-known feature predicted by von Neumann's (1943) two- and three-shock theories. Its experimental confirmation is

https://doi.org/10.1017/S0022112097005326 Published online by Cambridge University Press

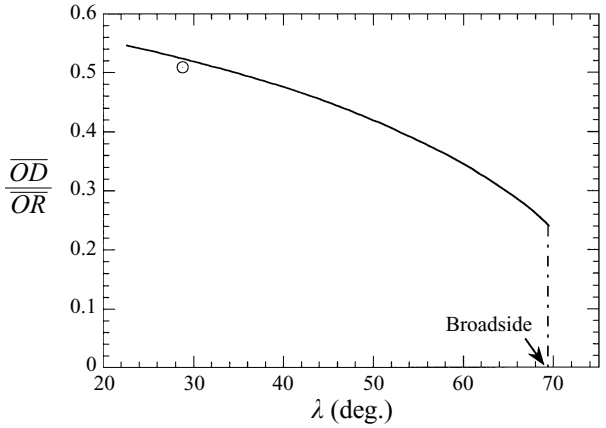


FIGURE 21. Dependence of the sonic front position $\overline{OD}/\overline{OR}$ on λ for $\theta_w = 11.2°$, $M_\infty = 5$ and $M_s = 1.24$. The open circle is a numerical result of Kutler *et al.* (1975).

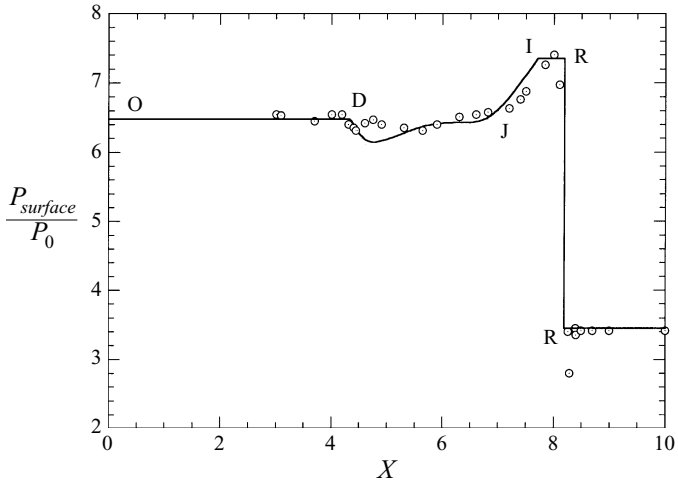


FIGURE 22. Surface pressure distribution for $\theta_w = 11.2°$, $M_\infty = 5$, $M_s = 1.24$ and $\lambda = 22.8°$. Open circles – numerical results of Kutler *et al.* (1975); solid line – present analytical results.

somewhat difficult because the peak pressure jump in an unsteady configuration may be of extremely short duration. The existence of a pressure jump contradicts the so-called *mechanical equilibrium* criterion for RR $\leftrightarrow$ MR transition (for details see Ben-Dor 1991). This jump predicted by the present model is greater than that predicted by the numerical simulation and smaller than that predicted by the approximate theory.

The relation between the original bow shock wave angle, β, and the new bow shock wave angle, β', in the (M_∞, M_s)-plane for a head-on S-O-S interaction ($\lambda = 0$) is shown in figure 20. It is evident that $\beta' > \beta$ for $M_\infty > 5$.

The dependence of the position of the sonic front $\overline{BD}$ (see figure 3*a*) on λ, for $\theta_w = 11.2°$, $M_\infty = 5$ and $M_s = 1.24$, is shown in figure 21. One numerical datum of Kutler *et al.* (1975) lies very close to the analytically predicted value.

The pressure distribution along the wedge surface is presented in figure 22. The wave configuration, for the given set of parameters, is a regular reflection. It is clear that a transient pressure pulse is introduced at the reflection point R, and that the maximum

https://doi.org/10.1017/S0022112097005326 Published online by Cambridge University Press

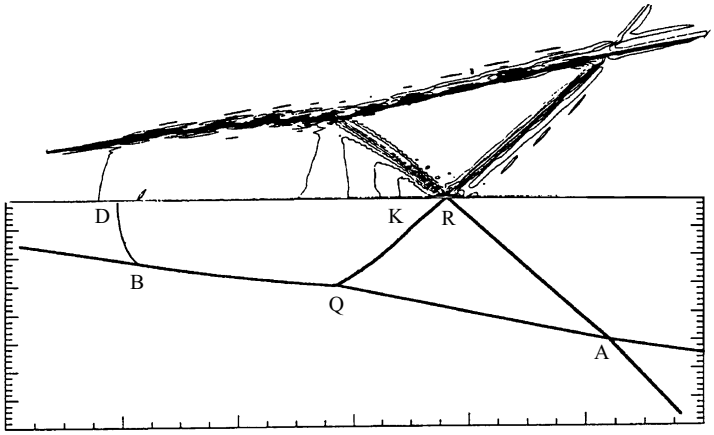


FIGURE 23. Comparison between the predicted wave configuration and the numerical simulation of Kutler *et al.* (1975) for $\lambda = 22.8°$, $\theta_w = 11.2°$; $M_\infty = 5$ and $M_s = 1.24$.

surface pressure is reached immediately behind it. Then the pressure remains constant, until point I, where the leading expansion wave reaches the wedge surface (see figure 3*a*). Then, the pressure drops monotonically to the value at point J, where the rear expansion wave reaches the wedge surface (see figure 3*a*). The location of points I and J can be determined from the following equations:

$$\frac{\overline{IR}}{\overline{OR}} = \frac{\sin\chi_k \sin[\phi_5(K)-\theta_5(K)+\mu_5(K)]}{\sin[\chi_K+\phi_5(R)-\theta_5(R)]\sin[\phi_5(K)-\theta_5(K)+\mu_5(K)-\phi_5(R)+\theta_5(R)]}, \tag{98}$$

$$\frac{\overline{JR}}{\overline{OR}} = \frac{\sin\chi_K \sin[\phi_5(K)-\theta_5(K)-\theta_7(K)+\mu_7(K)]}{\sin[\chi_K+\phi_5(R)-\theta_5(R)]\sin[\phi_5(K)-\theta_5(K)-\theta_7(K)+\mu_7(K)-\phi_5(R)+\theta_5(R)]}, \tag{99}$$

where $\mu_5(K) = \arcsin[1/M_5(K)]$ and $\mu_7(K) = \arcsin[1/M_7(K)]$.

The minimum surface pressure is obtained at the point at which the isobar line emanating from point C connects, which is located between points J and D. The accurate location of this minimum surface pressure point cannot be predicted by the present model. Instead, it was approximately determined by using an arc, which was assumed to have the same source centre as the sonic front, to connect it with point C. From the leading edge to the sonic front, the pressure remains constant. Comparison of Kutler's *et al.*'s (1975) numerical data with the present predicted results indicated that the agreement between them was, in general, very good except for the minimum pressure value.

A comparison of the analytically predicted wave configuration and the appropriate numerical simulation of Kutler *et al.* (1975) for $\lambda = 22.8°$, $\theta_w = 11.2°$, $M_\infty = 5$ and $M_s = 1.24$ is shown in figure 23. Good agreement is evident.

The above results and discussion are for the regular S-O-S interactions. Regarding the irregular S-O-S interactions, one should first determine the conditions for their existence, i.e. obtain the transition criterion between the regular and the irregular S-O-S interactions. The necessary conditions for the existence of a regular S-O-S interaction are $M_3(A) > 1$ and $M_4(A) > 1$, which means that point A is isolated from the downstream disturbance. It can be easily shown that

$$M_4(A) > M_3(A) \quad \text{if} \quad M_s < M_b,$$

and

$$M_3(A) > M_4(A) \quad \text{if} \quad M_s > M_b.$$

https://doi.org/10.1017/S0022112097005326 Published online by Cambridge University Press

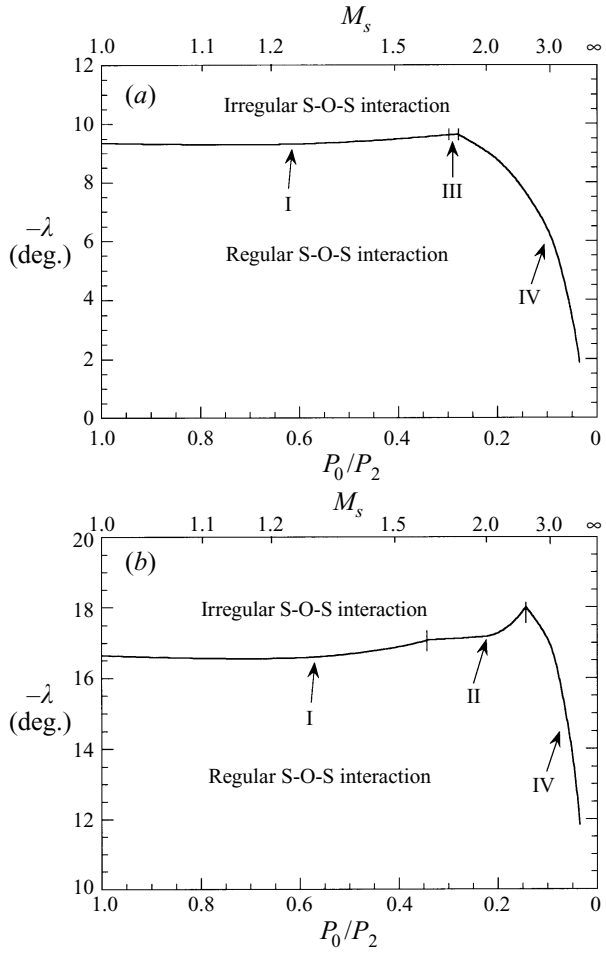


FIGURE 24. Regular to irregular S-O-S interaction transition criterion in the (λ, M_s)-plane for (*a*) $\theta_w = 11.2°$, $M_\infty = 5$, and (*b*) $\theta_w = 20°$, $M_\infty = 5$.

Here $M_b = M_\infty \sin\beta$ is the strength of the original bow shock wave (b). It is clear that $M_3(A) = M_4(A)$ only when $M_s = M_b$. Similar to the sonic RR $\leftrightarrow$ MR transition criterion, it is hypothesized here that the transition criterion between regular and irregular S-O-S interactions is $M_4(A) > M_3(A) = 1$ or $M_3(A) > M_4(A) = 1$. Furthermore, since the S-O-S interaction is associated with a wedge, the transmitted shock wave (t) must reflect over the wedge surface. If it inclines forward, i.e. $\omega > \frac{1}{2}\pi$, the reflection becomes impossible. Therefore, an additional necessary condition $\omega < \frac{1}{2}\pi$ is needed for a regular S-O-S interaction. Combining the above two requirements, the transition criteria can be summarized as

$$\left.\begin{array}{lll} \text{I} & M_4(A) > M_3(A) > 1, & \omega = \frac{1}{2}\pi \\ \text{II} & M_4(A) > M_3(A) = 1, & \omega < \frac{1}{2}\pi \end{array}\right\} \quad \text{for} \quad M_s < M_b,$$

$$\left.\begin{array}{lll} \text{III} & M_3(A) > M_4(A) > 1, & \omega = \frac{1}{2}\pi \\ \text{IV} & M_3(A) > M_4(A) = 1, & \omega < \frac{1}{2}\pi \end{array}\right\} \quad \text{for} \quad M_s > M_b.$$

The transition criteria in the (λ, M_s)-plane for $\theta_w = 11.2°$, $M_\infty = 5$ and $\theta_w = 20°$, $M_\infty = 5$, are shown in figures 24(*a*) and 24(*b*), respectively.

https://doi.org/10.1017/S0022112097005326 Published online by Cambridge University Press

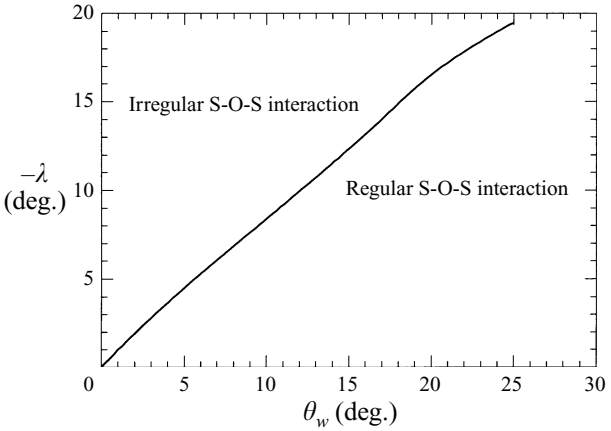


FIGURE 25. Regular to irregular S-O-S interaction transition criterion in the (λ, θ_w)-plane for $M_\infty = 5$ and $M_s = 1.2$.

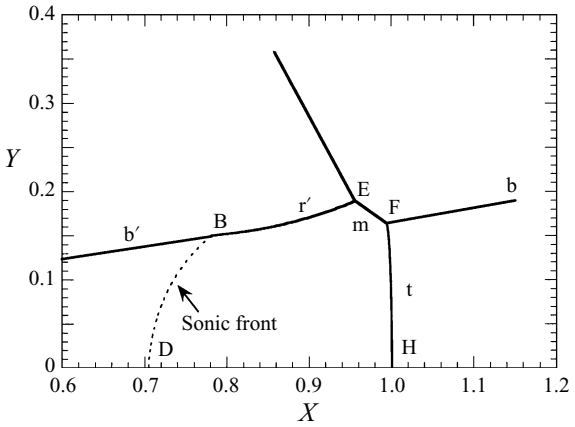


FIGURE 26. Predicted wave configuration of an irregular S-O-S interaction for $\lambda = -30°$, $\theta_w = 10°$, $M_\infty = 5$ and $M_s = 2$.

The transition criterion in the (λ, θ_w)-plane for $M_\infty = 5$ and $M_s = 1.2$ is shown in figure 25. It is important to note that irregular S-O-S interactions always occur for negative values of λ. In other words, head-on S-O-S interactions, for which $\lambda = 0$, cannot result in irregular S-O-S interactions. This finding contradicts Smyrl's (1963) hypotheses, who claimed that three different types of head-on S-O-S interactions are possible for a slender body ($\theta_w \ll 1$ rad), i.e. non-intersection tangents (regular), intersection tangents (regular), and single tangent (irregular). It should be mentioned here that neither Merritt & Aronson (1965) nor Brown & Mullaney (1965) recorded irregular S-O-S interaction cases when they conducted head-on S-O-S interaction experiments with a slender wedge and a cone.

Finally, a predicted irregular S-O-S interaction wave configuration is shown in figure 26. As expected, the Mach stem (m) is short, and the refracted bow shock wave (r′) is convex toward the wedge. This is due to the fact that a family of compression waves propagates towards region (6) (see figure 4) rather than a family of expansion waves which exists in regular S-O-S interaction (see figures 3*a* and 3*b*).

Similar to the regular S-O-S interaction case, the analytical model of the irregular

https://doi.org/10.1017/S0022112097005326 Published online by Cambridge University Press

S-O-S interaction should also be validated by comparing its predictions with experimental results. Unfortunately, however, to the best of the authors' knowledge, such experiments do not exist yet. The present analysis can help towards better understanding of shock wave irregular S-O-S interactions, which are considered more complicated than shock wave reflections since the former contain two unequal strength shock waves, and they propagate towards a non-quiescent gas.

As a final remark it should be noted that Kutler *et al.* (1975) found that their two-dimensional numerical results agreed well with three-dimensional (cone) experimental data, especially for the maximum surface pressure which is a major concern of the S-O-S interaction. Consequently, it is probable that the two-dimensional model developed here may also be applied to three-dimensional S-O-S interactions for which it is impossible to develop an analytical model since they contain non-uniform conical flow regions.

4. Conclusions

The unsteady inviscid two-dimensional flow field and the wave configurations, which result when a supersonic vehicle strikes a planar oblique shock wave, were modelled and analytically predicted. Based on the two- and three-shock theories, the geometric shock dynamics theory and some approximations and simplifying assumptions, both regular and irregular shock-on-shock (S-O-S) interactions were investigated, and the transition criterion between them was suggested. In the case of a regular S-O-S interaction, the transmitted shock wave reflects over the vehicle body surface either as a regular (RR) or a Mach reflection (MR) depending on the inclination angle and the strength of the impingement shock wave. A pronounced peak surface pressure jump was found to exist during the RR $\leftrightarrow$ MR transition. A RR $\leftrightarrow$ MR transition criterion for the case of a non-quiescent flow ahead of the shock pattern was proposed.

Compared with their experimental and numerical counterparts, analytical predictions are relatively easy to model. They result in a physical description of the wave pattern and the flow field including the peak surface pressure. The results based on the model developed here agree better than existing approximate theories with both experimental data and numerical simulations.

Finally, it should be noted that, to the best of the authors' knowledge, no numerical simulations have been published following those of Kutler *et al.* (1975) and Kutler & Sakell (1976). Consequently, a comparison of the present analytical predictions to simulations using state-of-the-art numerical codes is not possible at present.

REFERENCES

Ben-Dor, G. 1991 *Shock Wave Reflection Phenomena*. Springer.

Blankenship, V. D. 1964 Shock-shock interaction on a slender supersonic cone. *J. Fluid Mech.* **22**, 599–615.

Brown, E. A. & Mullaney, G. J. 1965 Experiments on the head-on shock-shock interaction. *AIAA J.* **3**, 2168–2170.

Han, Z. & Yin, X. 1993 *Shock Dynamics*. Kluwer.

Hudgins, H. E. & Friedman, E. M. 1973 Shock-shock interaction studies for weak incident shocks. *TR*-4590. Picatinny Arsenal, NJ, USA.

Inger, G. R. 1966 Blast wave impingement on the slender wedge moving at hypersonic speeds. *AIAA J.* **4**, 428–435.

Kutler, P. & Sakell, L. 1976 Three-dimensional shock-on-shock interaction problem. *AIAA J.* **13**, 1360–1367.

https://doi.org/10.1017/S0022112097005326 Published online by Cambridge University Press

Kutler, P., Sakell, L. & Aiello, G. 1975 Two-dimensional shock-on-shock interaction problem. *AIAA J*. **13**, 361–367.

Lagow, J. & Murad, P. 1975 A computerized model to predict the transient pressure distribution due to shock-shock interaction. *Martin-Marietta Aerospace*, *Orlando*, *FL*, *USA*.

Li, H. & Ben-Dor, G. 1995 Reconsideration of the shock-shock relations for the case of a non-quiescent gas ahead of the shock and verification with experiments. *Proc. R. Soc. Lond.* A **451**, 383–397.

Li, H., Ben-Dor, G. & Han, Z. Y. 1994 Analytical prediction of the reflected-diffracted shock wave shape in the interaction of a regular reflection with an expansive corner. *Fluid Dyn. Res*. **14**, 229–239.

Merritt, D. L. & Aronson, P. M. 1965 Study of blast-bow wave interaction in a wind tunnel. *AIAA Paper* 65-5.

Merritt, D. L. & Aronson, P. M. 1967 Wind tunnel simulation of head-on bow wave-blast wave interaction. *NOLTR* 67-123. Naval Ordnance Lab, White Oak, Maryland, USA.

Miles, J. W. 1965 A note on shock-shock diffraction. *J. Fluid Mech*. **22**, 95–102.

Miller, W. D., Schindel, L. & Ruetenik, J. R. 1964 Computer program for the calculation of the interaction of the blast wave with a non-uniform shock layer. *MIT Rep*. ASRL-TR-121-2. MIT, Cambridge, MA, USA.

Neumann, J. von 1943 Oblique reflection of shock. *Explos. Res. Rep*. 12. Navy Dept., Bureau of Ordinance, Washington, DC, USA (also *Collected Works*, Vol. 6, pp. 238–299, Pergamon).

Ruetenik, J. R., Cole, E. L. & Jones, R. E. 1973 Shock-on-shock pressure measurements at Mach 5 from rocket-propelled sled tests, phase I: lateral intercepts. *KAMAN AviDyne Rep*. KA TR-98. Kaman Aerospace Corp., Bloomfield, CN, USA.

Smyrl, J. L. 1963 The impact of a shock-wave on a thin two-dimensional aerofoil moving at supersonic speed. *J. Fluid Mech*. **15**, 223–240.

https://doi.org/10.1017/S0022112097005326 Published online by Cambridge University Press